Title

Individuals with progranulin haploinsufficiency exhibit features of neuronal ceroid lipofuscinosis

Journal

Science Translational Medicine, 9(385)

ISSN

1946-6234

Authors

Ward, Michael E

Chen, Robert

Huang, Hsin-Yi

et al.

Publication Date

2017-04-12

DOI

10.1126/scitranslmed.aah5642

Peer reviewed

NEURODEGENERATIVE DISEASE

Individuals with progranulin haploinsufficiency exhibit features of neuronal ceroid lipofuscinosis

Michael E. Ward,[1,2,3] Robert Chen,[1,3] Hsin-Yi Huang,[4,5] Connor Ludwig,[1,3] Maria Telpoukhovskaia,[1] Ali Taubes,[1] Helene Boudin,[4,6] Sakura S. Minami,[1] Meredith Reichert,[1] Philipp Albrecht,[7] Jeffrey M. Gelfand,[3] Andres Cruz-Herranz,[3] Christian Cordano,[3] Marcel V. Alavi,[8] Shannon Leslie,[1] William W. Seeley,[3] Bruce L. Miller,[3] Eileen Bigio,[9] Marek-Marsel Mesulam,[9] Matthew S. Bogyo,[10] Ian R. Mackenzie,[11] John F. Staropoli,[12] Susan L. Cotman,[12] Eric J. Huang,[4,13] Li Gan,[1,3]* Ari J. Green[3,8]*

Heterozygous mutations in the *GRN* gene lead to progranulin (PGRN) haploinsufficiency and cause frontotemporal dementia (FTD), a neurodegenerative syndrome of older adults. Homozygous *GRN* mutations, on the other hand, lead to complete PGRN loss and cause neuronal ceroid lipofuscinosis (NCL), a lysosomal storage disease usually seen in children. Given that the predominant clinical and pathological features of FTD and NCL are distinct, it is controversial whether the disease mechanisms associated with complete and partial PGRN loss are similar or distinct. We show that PGRN haploinsufficiency leads to NCL-like features in humans, some occurring before dementia onset. Noninvasive retinal imaging revealed preclinical retinal lipofuscinosis in heterozygous *GRN* mutation carriers. Increased lipofuscinosis and intracellular NCL-like storage material also occurred in postmortem cortex of heterozygous *GRN* mutation carriers. Lymphoblasts from heterozygous *GRN* mutation carriers accumulated prominent NCL-like storage material, which could be rescued by normalizing PGRN expression. Fibroblasts from heterozygous *GRN* mutation carriers showed impaired lysosomal protease activity. Our findings indicate that progranulin haploinsufficiency caused accumulation of NCL-like storage material and early retinal abnormalities in humans and implicate lysosomal dysfunction as a central disease process in *GRN*-associated FTD and *GRN*-associated NCL.

INTRODUCTION

Neurodegenerative diseases of adulthood are usually thought to occur via mechanisms distinct from those of childhood. Neuronal ceroid lipofuscinosis (NCL) is the most common neurodegenerative disease of childhood. Progranulin-related frontotemporal dementia (FTD), a neurodegenerative syndrome of older adults, is the most common cause of dementia in those <60 years old. Individuals affected by FTD usually present with behavioral changes, language difficulties, or motor symptoms (*1*). Heterozygous mutations in the progranulin (*GRN*) gene are common causes of familial FTD. Such mutations lead to progranulin (PGRN) haploinsufficiency, reducing PGRN expression by 60 to 70% via nonsense-mediated mRNA decay (*2*). PGRN has been reported to regulate numerous cellular processes, including cell survival, inflammation, and protein clearance (*3*–*12*). However, it is not understood why partial loss of PGRN causes neurodegeneration.

Recently, we discovered that retinal degeneration occurs in preclinical heterozygous *GRN* mutation carriers (*13*), a phenotype also observed in *Grn* knockout mice (*13*, *14*). *Grn* knockout mice also develop prominent deposits of autofluorescent aggregates known as lipofuscin throughout the central nervous system (CNS) (*7*, *15*, *16*). Ultrastructurally, this storage material bears a striking resemblance to storage material found in NCL, a disease clinically characterized by early vision loss and retinal atrophy. Individuals with homozygous *GRN* mutations develop a clinical syndrome consistent with NCL (vision loss followed by seizures and ataxia) (*17*–*19*). Electron microscopy (EM) analysis of lymphocytes from one of these subjects revealed NCL-like storage material (*18*).

Classically, NCL encompasses a family of related genetic syndromes with shared clinical and pathologic features, which together are the major cause of neurodegeneration in childhood. Vision loss is often an early clinical feature of NCL and can precede development of other neurological symptoms, which usually include seizures, ataxia, cognitive dysfunction, and early death (*20*). Most of the known mutations associated with NCL cause loss of function in genes necessary for normal lysosome function. In keeping with this, deposition of autofluorescent intralysosomal storage material known as lipofuscin is a pathological hallmark of NCL (*21*).

Although it is generally agreed that NCL can be caused by complete loss of PGRN, whether FTD caused by partial loss of PGRN shares similar clinical, pathological, or mechanistic features with NCL remains controversial. Unlike the *Grn* knockout mice, heterozygous *Grn* mice do not develop CNS lipofuscinosis (*7*). Furthermore, the classic clinical and pathological findings considered characteristic of *GRN*-associated FTD appear distinct from those in NCL (namely, early behavioral/language abnormalities with pathologic TDP-43 mislocalization in FTD versus vision loss, seizures, and ataxia with pathologic lipofuscin accumulation in NCL). However, a comprehensive evaluation of humans with PGRN haploinsufficiency for clinicopathological features of NCL has not been conducted.

On the basis of our previous observations of early retinal degeneration in humans with heterozygous *GRN* mutations—which could be consistent with an NCL phenotype—we suspected that other NCL-like

[1]Gladstone Institute of Neurological Disease, Gladstone Institutes, San Francisco, CA 94158 USA. [2]National Institute of Neurological Disorders and Stroke, National Institutes of Health, Bethesda, MD 20892, USA. [3]Department of Neurology, University of California, San Francisco, San Francisco, CA 94158 USA. [4]Department of Pathology, University of California, San Francisco, San Francisco, CA 94158, USA. [5]Department of Pathology, National Taiwan University Hospital, Taipei City, Taiwan. [6]INSERM UMR 913, Université de Nantes, Nantes, France. [7]Department of Neurology, Medical Faculty, Heinrich-Heine University Duesseldorf, Duesseldorf, Germany. [8]Department of Ophthalmology, University of California, San Francisco, San Francisco, CA 94158, USA. [9]Department of Pathology, Northwestern University Feinberg School of Medicine, Chicago, IL 60611, USA. [10]Department of Pathology, Stanford Medical School, Palo Alto, CA 94305, USA. [11]Department of Pathology and Laboratory Medicine, University of British Columbia, Vancouver, Canada. [12]Center for Human Genetic Research, Massachusetts General Hospital, Harvard Medical School, Boston, MA 02114, USA. [13]Pathology Service, Veterans Affairs Medical Center, San Francisco, CA 94141, USA.
*Corresponding author. Email: lgan@gladstone.ucsf.edu (L.G.); agreen@ucsf.edu (A.J.G.)

features may occur in these patients but may have been overlooked. We examined retinas of living presymptomatic heterozygous *GRN* mutation carriers by noninvasive autofluorescence imaging and analyzed postmortem cortical tissues from FTD subjects with heterozygous *GRN* mutations. In addition, we imaged lymphoblasts from heterozygous *GRN* mutation carriers and their normal siblings by EM to quantify NCL-like storage material. We enhanced PGRN expression in lymphocytes from heterozygous *GRN* mutation carriers to assess the effects of PGRN on NCL-like structures and storage material. Finally, we directly assessed lysosomal function in fibroblasts from heterozygous *GRN* mutation carriers. Our findings indicate that core clinicopathological features of NCL occur in humans with PGRN haploinsufficiency caused by heterozygous *GRN* mutations, implicating lysosomal dysfunction as a potential disease process in *GRN*-associated FTD.

RESULTS

Lipofuscinosis and NCL-like storage material in retinal neurons from Grn knockout mice

Vision loss is often the first symptom noticed by patients with some forms of NCL, and it is accompanied by retinal atrophy and deposition of autofluorescent lipofuscin. We reported retinal degeneration accompanied by electrophysiological dysfunction in *Grn* knockout mice (*13*), which was subsequently reported by others (*14*). Similar to findings in cortical neurons from *Grn* knockout mice and in various NCL animal models (*7*), we observed NCL-like lysosomal storage material in retinal neurons from *Grn* knockout mice (Fig. 1A).

Age-dependent autofluorescent lipofuscin deposition was observed throughout the retina in *Grn* knockout mice, reminiscent of autofluorescent lipofuscin deposits in NCL (Fig. 1, B and C). In addition, subretinal drusen-like autofluorescent deposits were higher in aged *Grn* knockout mice than in control animals: 16.0 + 2.7 versus 3.2 ± 1.9 deposits per retinal cross section ($n = 5$, $P < 0.001$, mixed-model linear regression). Pathologic retinal lipofuscinosis occurred in very young *Grn* knockout mice (1.5 months of age), preceding any other functional or degenerative phenotype in these animals (Fig. 1, C and D, and table S3) (*7*, *8*, *13*, *22*, *23*). Consistent with previous evaluations of the cortex (*7*), we did not see increased retinal lipofuscinosis in aged *Grn* $^{+/-}$ mice (figs. S1 and S2).

Noninvasive imaging of retinal autofluorescence is routinely performed in clinical settings with confocal scanning laser ophthalmoscopy (cSLO) and can be used to detect retinal lipofuscin deposits. To determine whether retinal lipofuscinosis secondary to PGRN deficiency can be imaged in vivo, we used a modified cSLO to image the retina of anesthetized *Grn* knockout mice. Similar to our observations in fixed tissue, we detected retinal lipofuscin using cSLO in *Grn* knockout mice (Fig. 1, E and F). We simultaneously imaged *Grn* knockout mice with spectral domain optical coherence tomography (OCT) to determine whether individual lipofuscin deposits could be localized to specific retinal layers. Although most autofluorescent deposits were below the resolution of OCT in mice, we did note occasional aggregates of subretinal deposits in *Grn* knockout mice, consistent with our pathological observations (Fig. 1E, insets).

Noninvasive imaging of retinal lipofuscin in heterozygous GRN mutation carriers by autofluorescent retinal imaging

We previously reported retinal thinning in humans with heterozygous *GRN* mutations (*13*). We used cSLO to image retinal autofluorescence in 11 heterozygous *GRN* mutation carriers and 22 age-matched and sex-matched healthy controls (tables S1 and S2). Retinal lipofuscinosis was seen more often in heterozygous *GRN* mutation carriers than in controls (Fig. 2, A to C). Most lipofuscin deposits were not visible on OCT scans through the same region (Fig. 2B). Occasional lipofuscin deposits correlated with subretinal drusen-like aggregates (Fig. 2C). Quantification of subretinal drusen revealed a trend toward increased drusen per eye in *GRN* mutation carriers, but this was not statistically significant (table S2). Heterozygous *GRN* mutation carriers were about twice as likely to have retinal lipofuscin deposits than controls (Fig. 2D and tables S1 and S3). In addition, both the average number and the area of lipofuscin deposits were substantially greater in *GRN* mutation carriers (Fig. 2, E and F), including those who were clinically asymptomatic (Fig. 2, E and F).

Increased storage material in postmortem cortex of heterozygous GRN mutation carriers

We next asked whether storage material deposition also occurred in the frontal cortex of heterozygous *GRN* mutation carriers, because degeneration of this region of the CNS causes many of the clinical symptoms of FTD. Formalin-fixed postmortem human cortex samples from 15 *GRN* mutation carriers, 16 nondemented control subjects, and 6 Alzheimer's disease (AD) subjects were imaged by EM. We noted a marked increase in storage material accumulation in cortical neurons of *GRN* mutation carriers but not AD subjects compared to nondemented controls (Fig. 2, G and H). Morphologically, the storage material found in the formalin-fixed postmortem cortex from *GRN* mutation carriers resembled granular osmiophilic deposits. Such deposits occur in a broad range of NCL subtypes, including recessive infantile-onset forms caused by *PPT1* mutations (NCL type 1) and an adult-onset form caused by dominant mutations in *DNAJC5* (NCL type 4). Both the percentage of neurons that contained storage material and the number of storage material deposits per neuron were increased in heterozygous *GRN* mutation carriers (Fig. 2H). Storage material was also present in microglia in heterozygous *GRN* mutation carriers (fig. S3). We did not observe an increase in NCL-like storage material in postmortem cervical spinal cord tissue from heterozygous *GRN* mutation carriers, an area of the CNS that does not typically degenerate in *GRN*-related neurodegeneration (fig. S4). Consistent with the results from EM, we observed an increase in autofluorescent lipofuscin deposits in the frontal cortex tissue from *GRN* mutation carriers by fluorescence microscopy (Fig. 2I). Lipofuscin staining using Sudan black showed a similar result (Fig. 2, J and K).

NCL-like storage material in lymphoblasts from heterozygous GRN mutation carriers

The presence of intracellular storage material with characteristic ultrastructural patterns is a defining pathological feature of NCL. Such storage material accumulates in neurons and certain non-neuronal cells in NCL patients. Evaluation of peripheral blood lymphocytes for storage material is commonly performed in clinical settings when a diagnosis of NCL is under consideration. Recently, a patient diagnosed with NCL was posthumously found to carry a heterozygous *GRN* mutation (c.1477C>T pArg493X), but neither electron micrographs nor tissue samples were available at the time to confirm the original diagnosis (*17*). We obtained lymphoblasts that had been banked from this patient and processed them for EM to evaluate the presence or absence of NCL-like storage material. We simultaneously evaluated lymphoblasts from a healthy individual and a patient with juvenile NCL (*CLN3* homozygous ~1-kb deletion). As expected, lymphoblasts carrying a *CLN3* mutation had numerous enlarged vacuolated structures, many containing multilamellar fingerprint profile patterns or onion skin-like storage material (Fig. 3A).

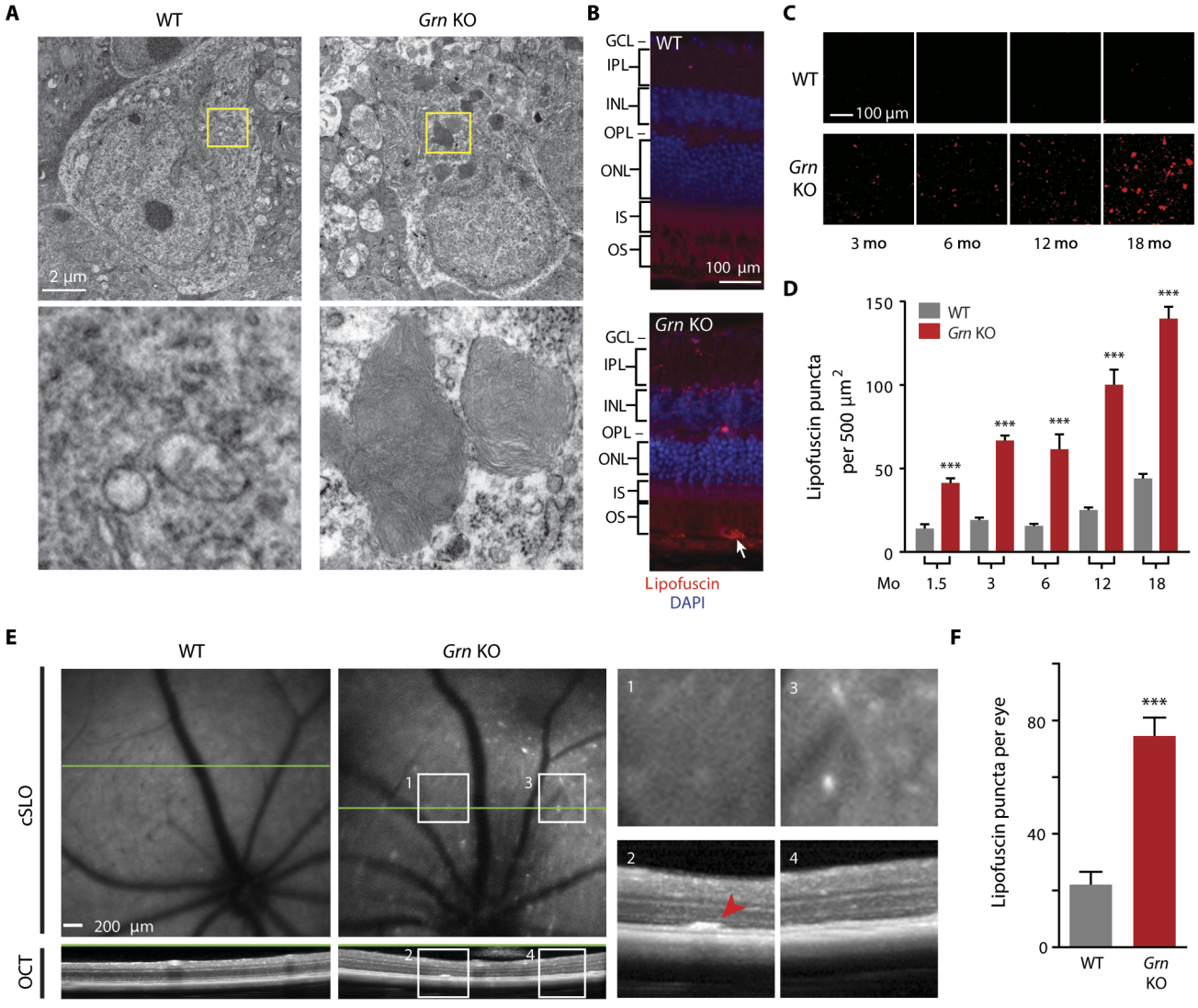

Fig. 1. Retinal NCL-like storage material and lipofuscinosis in *Grn* knockout mice. (**A**) Representative EM images of retinal ganglion cell layer (GCL) neurons from 18-month-old wild-type (WT) and *Grn* knockout (*Grn* KO) mice. Note the characteristic fingerprint profile patterns of NCL-like storage material (*Grn* KO, inset). (**B**) Representative retinal cross section from 24-month-old *Grn* KO mice showing autofluorescent lipofuscin throughout the retina. Especially prominent lipofuscinosis occurs in the GCL, inner nuclear layer (INL), deep layers of the inner plexiform layer (IPL), outer plexiform layer (OPL), and outer nuclear layer (ONL). Additionally, subretinal drusen-like autofluorescent aggregates occurred in *Grn* KO mice (white arrow). DAPI, 4′,6-diamidino-2-phenylindole; IS, inner segment; OS, outer segment. (**C**) Representative lipofuscin deposits (red puncta) in retinal whole mounts from aging WT and *Grn* KO mice. (**D**) Quantification of lipofuscin deposits from (C) $n = 4$ to 26 mice per age per genotype. ***$P < 0.001$, one-way analysis of variance (ANOVA) with Tukey's post hoc test. (**E**) Representative images of retinal lipofuscin in *Grn* KO mice imaged in vivo using cSLO. Green lines overlaid on cSLO images indicate the location of cross-sectional OCT scans. Occasional subretinal drusen-like deposits were observed in *Grn* KO mice (insets 1 and 2, red arrow), but most autofluorescent puncta were below the limit of detection of OCT cross-sectional scans through the same area (insets 3 and 4). (**F**) Quantification of in vivo imaging of retinal lipofuscin from (E). $n = 11$ to 12 eyes from six mice per genotype. ***$P < 0.001$, mixed-effect multivariate linear regression model.

Strikingly, lymphoblasts from the heterozygous *GRN* mutation carrier had prominent vacuolated structures containing storage material that was morphologically similar to that found in lymphoblasts carrying the *CLN3* mutation. Storage material was largely absent in lymphoblasts from a healthy control (Fig. 3A, inset)

We next asked whether NCL-like storage material also occurred in heterozygous *GRN* mutation carriers lacking a clinical diagnosis of NCL. We cultured lymphoblasts from five heterozygous *GRN* mutation carriers and processed them for EM. Siblings with WT *GRN* alleles of similar age served as controls. Lymphoblasts from these *GRN* mutation carriers had membrane-bound multilamellar NCL-like storage material deposits, similar in morphology to the *GRN* mutation carrier clinically diagnosed with NCL (fig. S5A). When analyzed as a group, we saw more storage material in lymphoblasts from *GRN* mutation carriers than in those from controls (Fig. 3B). When analyzed as matched sibling pairs, three of the *GRN* mutation carriers had lymphoblasts with more storage material than their control siblings (fig. S5, B and C). A similar but less pronounced difference was observed in the other two pairs (fig. S5, B and C).

Reduced NCL-like storage material in lymphoblasts from GRN mutation carriers treated with PGRN-expressing retrovirus

We next determined whether the NCL-like storage material phenotype in lymphoblasts from *GRN* mutation carriers could be rescued by increasing

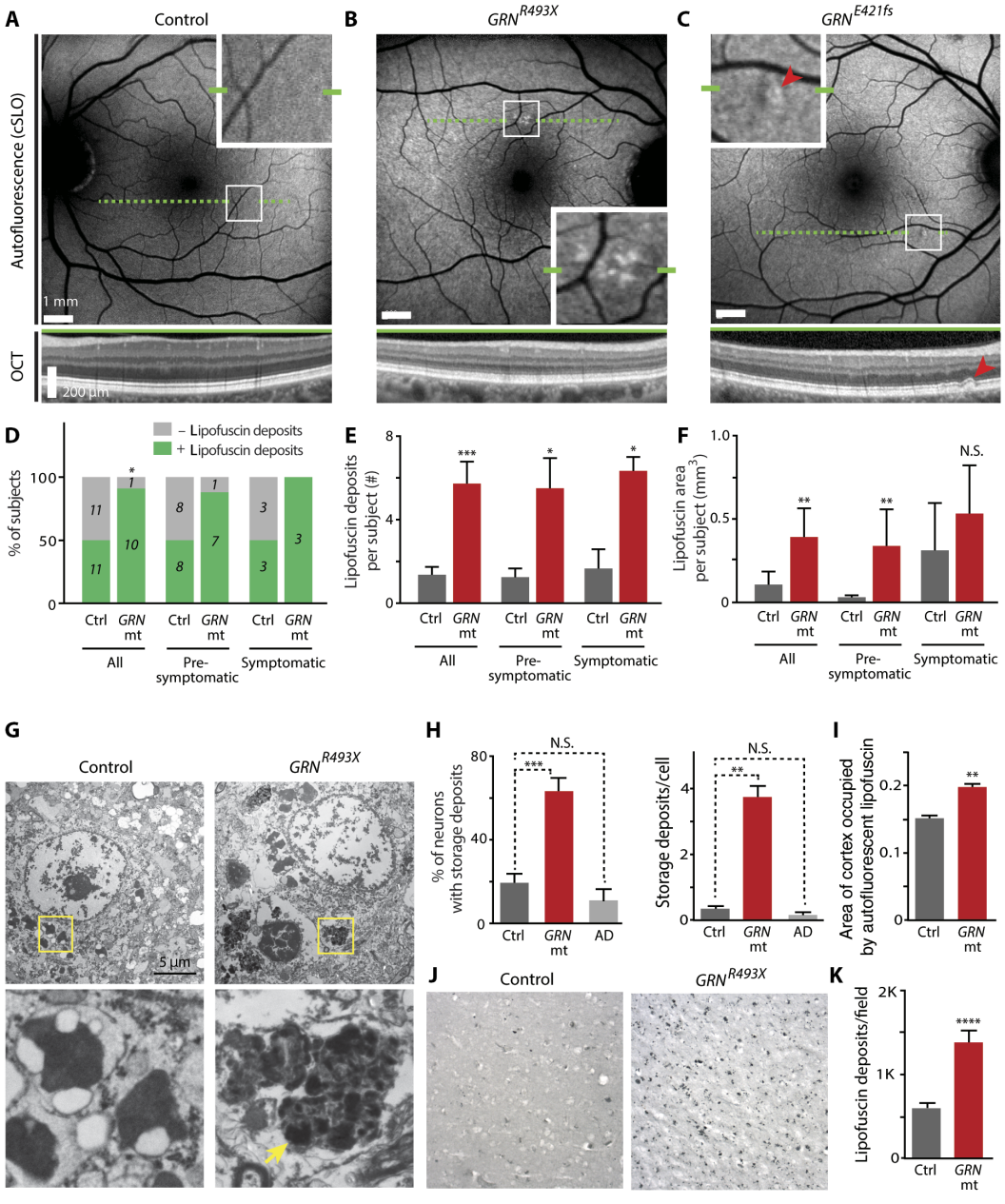

Fig. 2. Autofluorescent NCL-like storage material in the CNS of humans with heterozygous *GRN* mutations. (**A** to **C**) In vivo imaging of retinal lipofuscinosis in humans with *GRN* haploinsufficiency. Representative images of cSLO autofluorescent retinal imaging of one control subject (Ctrl) and two *GRN* mutation carriers (GRN mt) are shown. OCT cross-sectional scans (green dashed lines) are shown below the autofluorescent images. Lipofuscin deposits (insets) occurred more frequently in *GRN* mutation carriers than in control subjects. Most lipofuscin deposits did not correlate with detectable abnormalities in OCT cross-sectional scans (B), although some correlated with subretinal drusen-like material (C, red arrows). Scale bars, 1 mm. (**D** to **F**) Blinded quantification of retinal autofluorescence images obtained by cSLO. Data are grouped by all *GRN* mutation subjects versus all controls (n = 11 and 22), presymptomatic *GRN* mutation subjects versus matched controls (n = 8 and 16), and symptomatic *GRN* mutation subjects versus matched controls (n = 3 and 6). (D) Heterozygous *GRN* mutation carriers were more likely than controls to have retinal lipofuscin deposits; P = 0.027, Fisher's exact test. Asymptomatic and symptomatic *GRN* mutation carriers also were more frequently found to have retinal lipofuscin deposits, although the difference was not significant. P = 0.18 and 0.46, respectively, Fisher's exact test. The number of affected subjects is shown inside the bars. *P < 0.05. (E) Quantification of the total number of retinal lipofuscin deposits per subject. Heterozygous *GRN* mutation carriers had more lipofuscin deposits than did controls, including subgroups of asymptomatic and symptomatic *GRN* mutation carriers. *P <0.05, ***P < 0.001, Mann-Whitney U test. (F) Quantification of the total area of retinal lipofuscin deposits per subject. Heterozygous *GRN* mutation carriers had a greater total area of lipofuscin deposits than did controls, including a subgroup of asymptomatic *GRN* mutation carriers. **P < 0.01, Mann-Whitney U test. N.S., not significant. (**G**) Increased accumulation of electron-dense storage material in postmortem cortical tissue from heterozygous *GRN* mutation carriers. Shown are representative electron micrographs of formalin-fixed frontal cortex from control and heterozygous *GRN* mutation carriers. Note the presence of granular osmiophilic deposit–like storage material in neurons in cortical tissue from *GRN* mutation carriers (insets, yellow arrow), which was rarely observed in control cortical neurons. (**H**) Quantification of electron-dense storage material seen in (G). The percentage of neurons that contained such storage material and the number of deposits per neuron are shown. n = 4 to 26 neurons from 15 *GRN* mutation carriers, 16 control subjects, and 6 AD subjects. Percentage of neurons: ***P < 0.001, one-way ANOVA with Bonferroni's multiple comparison test; number of deposits per cell: **P < 0.001, mixed model linear regression. (**I**) Increased autofluorescent lipofuscin aggregates in postmortem cortical tissue from heterozygous *GRN* mutation carriers. n = 6 to 30 fields of view from nine *GRN* mutation carriers and nine controls; **P = 0.009, mixed-model linear regression. (**J**) Representative bright-field images of frontal cortex showing an increase in Sudan black–stained lipofuscin in postmortem cortical tissue from a heterozygous *GRN* mutation carrier versus control. (**K**) Quantification of Sudan black staining seen in (J). The number of lipofuscin deposits per field of view is shown. n = 10 *GRN* mutation carriers and 14 control subjects; ****P < 0.0001, Student's t test. Means ± SEM are shown in (E), (F), (H), (I), and (K).

PGRN expression in these cells. A PGRN-expressing retrovirus was used to transduce lymphoblasts carrying the $GRN^{V200GfsX18}$ mutation to increase PGRN expression to WT levels or higher (Fig. 3, C and D, and table S3). The NCL-like storage material was reduced in $GRN^{V200GfsX18}$ lymphoblasts infected with PGRN-expressing retrovirus compared to control cells transduced with an empty retrovirus (Fig. 3, E to G).

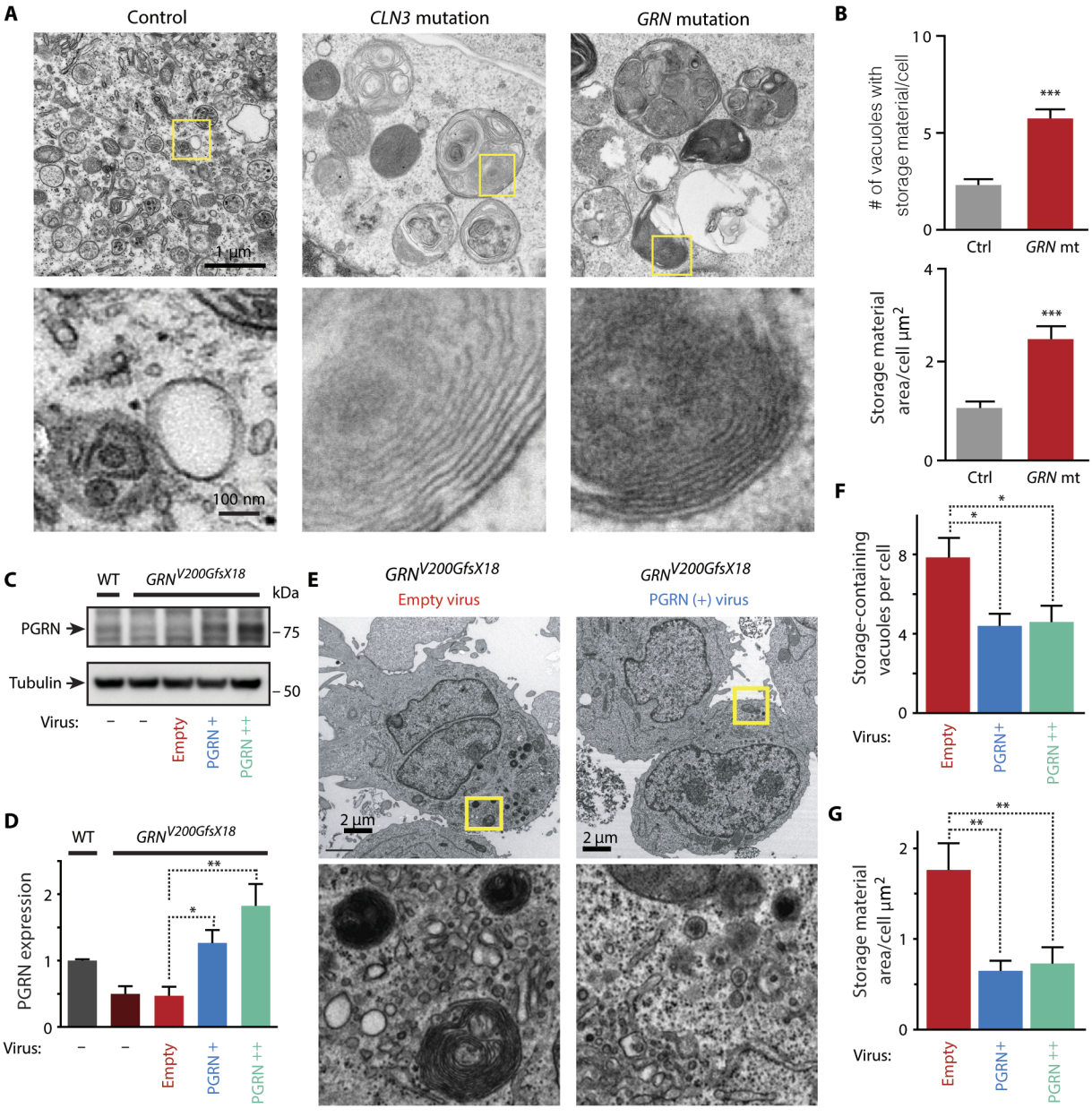

Fig. 3. *GRN* haploinsufficiency results in NCL-like storage material in lymphoblasts. (**A**) NCL-like storage material accumulates in lymphoblasts from a heterozygous *GRN* mutation carrier who clinically presented with NCL symptoms. Representative images of lymphoblasts from a healthy non–mutation-carrying control subject, an NCL patient (homozygous *CLN3* mutation carrier), and a heterozygous *GRN* mutation carrier are shown. Note the similar ultrastructural patterns of the storage material observed in the *CLN3* mutation carrier and the *GRN* mutation carrier, consisting of prominent vacuolated structures containing storage material with a fingerprint profile pattern (insets). (**B**) Quantification of NCL-like storage material in lymphoblasts from heterozygous *GRN* mutation carriers without clinical evidence of NCL versus noncarrier sibling controls. Five paired sets of lymphoblasts from control and heterozygous *GRN* mutation siblings were imaged with EM, and the number of vacuoles with storage material per cell and cross-sectional area occupied by storage material containing vacuoles was quantified in a blinded manner. $n = 19$ to 38 cells per subject from five pairs of *GRN* mutation carrier and control subjects; $^{***}P < 0.001$ via mixed-effect multivariate linear regression model. (**C** to **G**) Restoring normal PGRN expression in lymphoblasts from heterozygous *GRN* mutation carriers rescued the NCL-like storage material phenotype. (C) Western blot of intracellular PGRN and tubulin showing reduced expression of PGRN in heterozygous $GRN^{Exon\ 8\ (IVS7\text{-}1g)}$ mutation carrier lymphoblasts, which was rescued by treatment with a PGRN-expressing retrovirus. Control (empty vector) retrovirus did not alter PGRN expression. $GRN^{Exon\ 8\ (IVS7\text{-}1g)}$ mutation carrier lymphoblasts transduced with the PGRN-retrovirus that expressed PGRN at two different levels (endogenous, +; high, ++) were used for EM analysis. (D) Quantification of PGRN expression (normalized to tubulin). $n = 3$ wells per group; $^{*}P < 0.05$, $^{**}P < 0.01$, one-way ANOVA with Sidak's multiple comparison test. (E) Representative electron micrographs of heterozygous $GRN^{Exon\ 8\ (IVS7\text{-}1g)}$ mutation carrier lymphoblasts transduced with control (empty vector) or huPGRN retrovirus expressing PGRN at an endogenous level. Lymphoblasts transduced with PGRN-expressing retrovirus had less storage material than did those that were treated with empty vector (insets). (F and G) Quantification of the number of vacuoles with storage material per lymphoblast (F) or total cross-sectional area of storage material per lymphoblast (G) in lymphoblasts transduced with control or PGRN-expressing retrovirus. $n = 45$ to 65 cells per group, $^{*}P < 0.05$, $^{**}P < 0.01$, one-way ANOVA with Sidak's multiple comparison test. Means ± SEM are shown (B, D, F, and G).

Impaired lysosomal function in fibroblasts from heterozygous GRN mutation carriers

In NCL, lipofuscin accumulation is thought to be the pathological consequence of dysfunctional lysosomal proteolysis. We directly assessed lysosomal protease activity in human fibroblasts from heterozygous *GRN* mutation carriers and control siblings. We measured the activity of cysteine cathepsin proteases in living patient fibroblasts using a quenched fluorescent activity–based probe (*24*) and found that cathepsin activity in fibroblasts from *GRN* mutation carriers was reduced by ~40% compared to that in fibroblasts from control siblings (Fig. 4, A and B, fig. S6A, and table S3). We also saw reduced cathepsin D activity in fibroblast lysates from *GRN* mutation carriers (Fig. 4C and fig. S6B).

DISCUSSION

Our study shows that FTD caused by PGRN haploinsufficiency shares several fundamental clinicopathological features with NCL. Similar to other areas of the CNS, lipofuscin deposits formed in the retina in *Grn* knockout mice in a panretinal pattern similar to that seen in human NCL. Retinal lipofuscin deposition was an early phenotype in these mice, preceding neuron loss, and could be imaged in vivo. Retinal lipofuscin deposits also occurred in humans with heterozygous *GRN* mutations, including cognitively normal individuals, and could be detected with imaging technology used in clinical settings. Autofluorescent NCL-like storage material was present in the frontal cortex of human subjects with heterozygous *GRN* mutations. EM analysis of lymphoblasts from heterozygous *GRN* mutation carriers revealed the presence of NCL-like storage material, regardless of whether their clinical syndrome had NCL-like features. Transduction of lymphoblasts from *GRN* mutation carriers with PGRN-expressing retrovirus reduced storage material accumulation. Finally, lysosomal protease activity was impaired in fibroblasts from heterozygous *GRN* mutation carriers.

Whereas patients with homozygous *GRN* mutations have a clinical syndrome that closely resembles NCL, those with heterozygous *GRN* mutations usually present with FTD. Because the primary symptoms and pathological features of FTD and NCL are distinct, homozygous and heterozygous *GRN* mutations may cause neurodegeneration via divergent pathophysiological processes (*17*). In contrast, our study provides direct evidence that core clinicopathological phenotypes of NCL occur in heterozygous *GRN* mutation carriers. Vision loss and retinal atrophy are early phenotypes in most patients with NCL. Our recent observations of moderate retinal thinning in heterozygous *GRN* mutation carriers, compared to nearly complete vision loss and severe retinal atrophy in homozygous *GRN* mutation carriers (*18*), suggest a relationship between *GRN* gene dosage and the severity of retinal involvement. We also found that lipofuscinosis and membrane-bound storage material deposition—pathologic hallmarks of NCL—occurred in heterozygous *GRN* mutation carriers, consistent with what has been seen in homozygous *GRN* mutation carriers. A recent finding that an NCL case caused by a homozygous *GRN* mutation segregated in a family with neuropathologically confirmed FTLD further supports the notion that PGRN-deficient NCL and FTLD are pathophysiologically related (*19*).

On the basis of our findings, we propose that neurodegeneration is driven by a common central mechanism in both homozygous and heterozygous *GRN* mutation carriers but that the specific clinical syndrome is driven by *GRN* gene dosage. In homozygous *GRN* mutation carriers with complete PGRN loss, disease onset is in early adulthood and NCL symptoms predominate. In heterozygous *GRN* mutation carriers with partial PGRN loss, subclinical NCL features (such as retinal thinning) are present, but disease onset is in late adulthood and cognitive symptoms predominate. Additional subclinical features could also occur in heterozygous *GRN* mutation carriers that would require further investigation to detect. For example, although motor seizures are not commonly reported in *GRN*-associated FTD, prolonged electroencephalography might reveal subclinical epileptiform activity, similar to that seen in subjects with AD

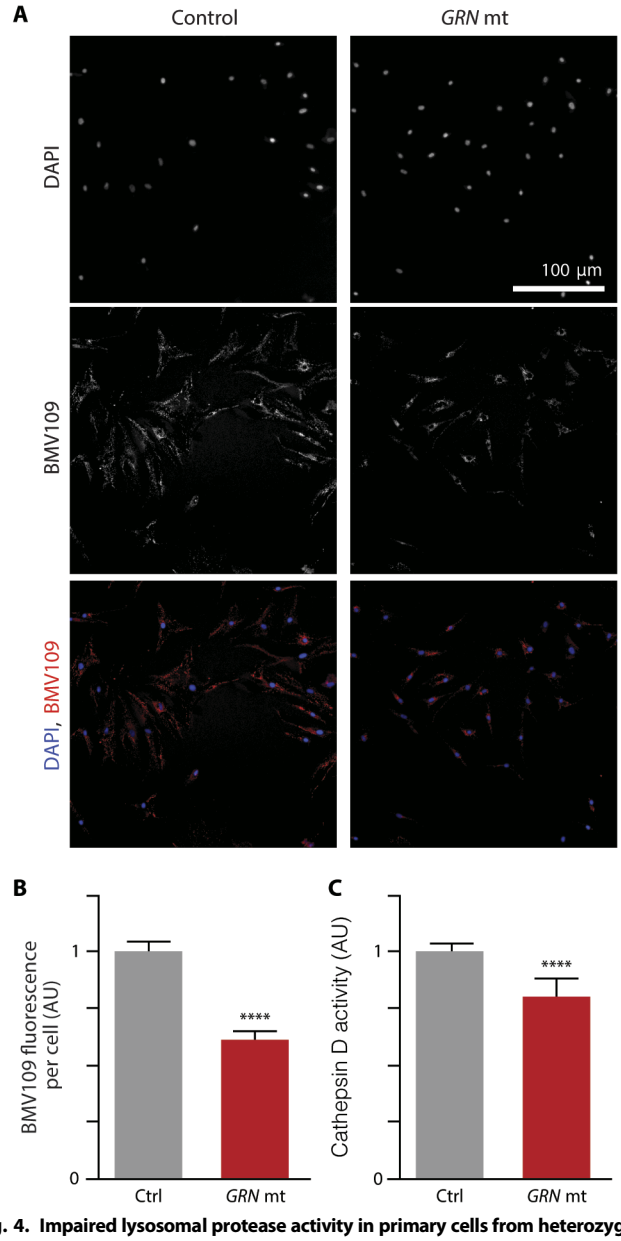

Fig. 4. Impaired lysosomal protease activity in primary cells from heterozygous *GRN* mutation carriers. (**A**) Representative images of fluorescence after staining with BMV109 (red), a cell-permeable probe for active cysteine cathepsin proteases, in HDFs from heterozygous *GRN* mutation carrier and control siblings (blue, DAPI nuclear stain). (**B**) Quantification of BMV109 fluorescence in heterozygous *GRN* mutation carrier and control HDFs. $n = 6$ wells imaged per HDF line from three pairs of *GRN* mutation carrier and matched sibling controls; $^{****}P < 0.0001$ via mixed-effect multivariate linear regression model. AU, arbitrary units. (**C**) Cathepsin D enzyme activity in HDF lysates from heterozygous *GRN* mutation carrier and control sibling pairs. $n = 10$ assays per HDF line from three pairs of *GRN* mutation carrier and matched sibling controls; $^{****}P < 0.0001$ via mixed-effect multivariate linear regression. Mean enzyme activity, normalized to matched sibling control lines, ±SEM is shown (B and C).

(*25*). Other symptoms seen in homozygous *GRN* carriers, such as cerebellar dysfunction, have not been documented in heterozygous *GRN* mutation carriers. One possible explanation is that such symptoms can be notoriously difficult to detect in clinical settings when they are subtle and difficult to localize, for example, behavioral manifestations of cerebellar dysfunction. Also, potential cerebellar pathology is not always assessed in these cases at autopsy. It will therefore be of interest to determine whether structural changes to the cerebellum occur in these individuals, for example, through assessment of cerebellar volume loss or changes in neural tracts as evidence of disruption of normal cerebellar input/output. It remains unclear why heterozygous PGRN-deficient mice failed to exhibit NCL-like pathology, despite striking NCL-like pathology in *Grn* knockout mice. It is possible that mice do not live long enough to develop such pathology or that additional genetic modifiers are required for NCL-like pathology to emerge, for example, disease-related *TMEM106b* polymorphisms.

Notably, we observed NCL-like storage material in a heterozygous *GRN* mutation carrier who presented with symptoms compatible with late-stage NCL, for example, limb dystonia, gait abnormalities, and spasticity at the age of 46. Because whole-genome sequencing is more broadly used to assist in the diagnosis of unusual neurological cases, additional atypical clinical presentations of heterozygous *GRN* mutation carriers may be discovered. Alternatively, this subject may have had additional partial loss-of-function sequence variants in NCL-related genes that pushed their clinical syndrome toward an NCL-like phenotype.

PGRN has been reported to regulate a diverse range of cellular functions, including cell proliferation, cell survival, tumor invasion, protein turnover, inflammation, and synaptic plasticity, and more recently, lysosomal function. It has been unclear which of these functions is directly regulated by PGRN, and numerous mechanisms have been proposed to explain how partial PGRN loss causes FTD. PGRN is a secreted glycoprotein and, in neurons, localizes predominantly to endolysosomes (*26*). It binds directly to sortilin, a transmembrane receptor involved in receptor scavenging and protein trafficking from the Golgi to the lysosomes (*26*). In addition, mutations in the *TMEM106b* gene markedly influence the age of onset of FTD in heterozygous *GRN* mutation carriers (*27*, *28*). TMEM106b localizes to endolysosomes and may regulate vesicular transport (*29*). On the basis of our observations of NCL-like phenotypes in heterozygous *GRN* mutation carriers, we propose that endolysosomal dysregulation is a potential central mechanism underlying neurodegeneration in humans with PGRN-deficient FTD.

Because nearly all heterozygous *GRN* mutations cause FTD through loss of PGRN expression, it has been speculated that increasing PGRN in *GRN* mutation carriers using therapeutic interventions should alter disease progression. However, one significant challenge in the development of effective therapeutics in FTD has been a lack of markers to monitor relevant pathophysiological processes. We found that PGRN-deficient lymphoblasts had increased NCL-like storage material and that increasing PGRN in these cells could rescue this phenotype, supporting a possible causal role of PGRN deficiency in endolysosomal dysfunction. It is largely accepted that the pathological accumulation of lipofuscin in NCL indicates ongoing endolysosomal dysfunction, but future studies are needed to clarify whether lipofuscin accumulation itself is pathogenic.

Our study further suggests that autofluorescent retinal imaging may have potential utility for *GRN* mutation carriers. Longitudinal autofluorescent retinal imaging could be an inexpensive, rapid, and noninvasive means of monitoring lipofuscinosis in the CNS, especially when paired with OCT analysis of retinal tissue loss in *GRN* mutation carriers. Future proof-of-concept studies in *Grn* knockout mice using serial in vivo retinal imaging could inform whether normalization of PGRN expression clears existing lipofuscin, slows future lipofuscin accumulation, and prevents retinal neuronal loss. Adaptation of OCT acquisition protocols may also permit the detection of abnormalities other than the subretinal deposits identified here.

It is important to note the limitations associated with this study. We found that PGRN-deficient lymphoblasts had increased NCL-like storage material and that increasing PGRN in these cells could rescue this phenotype. However, EM analysis of NCL-like storage material in lymphoblasts is too labor-intensive to be used in the clinic. It remains to be established whether other assays of impaired lysosome function in PGRN-deficient lymphoblasts could be used to measure disease progression or efficacy of potential treatments. We observed a robust difference in lipofuscin deposition in the retina and CNS of a single cohort of *GRN* mutation carriers compared to healthy controls. However, given their lack of specificity, these differences would not be sufficient for identification of presymptomatic individuals without an additional risk assessment, that is, genetics or family history. Replication of our findings in an independent cohort of *GRN* mutation carriers would reinforce our conclusions.

MATERIALS AND METHODS

Study design

The overall aim of the study was to determine whether cells and tissue from heterozygous *GRN* mutation carriers exhibited evidence of NCL-like accumulation of lysosomal storage material and lysosomal dysfunction. The objective of the first portion of the study was to determine whether NCL-like storage material occurred in *Grn* knockout mice using EM, histology, and live imaging techniques. The objective of the second portion of the study was to determine whether NCL-like storage material was present in the CNS of heterozygous *GRN* mutation carriers using retinal imaging of living subjects and analysis of postmortem human cortical tissue by EM. Subjects with heterozygous *GRN* mutations and age-matched and sex-matched control subjects without known neurological diseases were enrolled in the study through the University of California, San Francisco (UCSF) Memory and Aging Center in 2011–2014 as part of a larger study to evaluate retinal manifestations of neurodegenerative diseases. Predefined exclusion criteria included a history of ophthalmologic disease, including glaucoma, age-related macular degeneration (AMD), diabetic retinopathy, and ocular surgery (except cataract surgery). One *GRN* mutation carrier had AMD (dry) and was excluded from the analysis; the remainder did not have any of the above exclusion criteria. *GRN* mutation carriers also underwent a standardized neurological evaluation by a board-certified neurologist with fellowship training in behavioral neurology. Clinical disease rating (CDR) scores were assigned to each subject on the basis of the result of this evaluation. For the purposes of this study, subjects were classified as asymptomatic (CDR = 0) or symptomatic (CDR > 0). Written informed consent was obtained from all participants with capacity. In those unable to provide informed consent because of diminished capacity, assent was obtained from the participant and written consent was obtained from a designated surrogate decision-maker. The study protocol was approved by the UCSF Committee on Human Research [IRB (Institutional Review Board) #11-05333]. The objective of the third portion of the study was to evaluate primary cells from heterozygous *GRN* mutation carriers for evidence of lysosomal dysfunction using EM analysis of storage material accumulation and functional readouts of lysosomal hydrolase activity. All data were included (there was no outlier exclusion).

Lymphoblast analysis

Epstein-Barr virus–transformed lymphocytes from deidentified human subjects were grown in RPMI + 10% fetal calf serum + 1% penicillin/streptomycin. Equal numbers of cells from each line were seeded into 10 ml of medium in T75 tissue culture flasks, and medium was doubled in volume each time cells reached saturation (determined by medium pH) until the total volume was 40 ml. Cells were again allowed to expand until saturation density and were then pelleted and gently resuspended in ice-cold EM fixative [2.5% glutaraldehyde, 2% paraformaldehyde, and 0.025% calcium chloride, in a 0.1 M sodium cacodylate buffer (pH 7.4)]. After a 15-min incubation in fixative on ice, cells were repelleted at 5000 rpm in a swinging-bucket rotor centrifuge for 10 min at 4°C. The fixative was removed, and fresh fixative was gently layered on top of the cell pellet. Samples were centrifuged again at 5000 rpm for 10 min at 4°C and then processed further for EM.

Retroviral transduction of lymphoblasts

Untagged human progranulin was cloned into a murine stem cell virus (MSCV) backbone vector that coexpressed mRuby as a fluorescent marker, with an empty vector serving as a control. 293T cells were co-transfected with the MSCV vector and pCL-Ampho via Lipofectamine 2000, and viral supernatant was collected 2 days later and filtered through a 0.45-μm filter. *GRN* mutation lymphoblasts were resuspended in empty vector or PGRN-expressing retroviral supernatant and monitored for expression via fluorescence microscopy. PGRN-expressing cells were sorted into two groups by fluorescence-activated cell sorting: "high PGRN-expressing" cells were the brightest 5% of cells sorted, and "low PGRN-expressing" cells were the remaining mRuby-positive cells. These groups were then expanded in parallel as described above and processed for EM.

Electron microscopy

Lymphoblast pellets were generated as described above, mouse retinal tissue was fixed directly after harvest in EM fixative. Formalin-fixed postmortem human cortex was postfixed in EM fixative before further processing. For lymphoblasts and retinal tissue, subsequent processing was performed in a Leica Lynx automatic tissue processor. Briefly, the tissue was postfixed in osmium tetroxide, stained en bloc with uranyl acetate, dehydrated in graded ethanol solutions, infiltrated with propylene oxide/Epon mixtures, embedded in pure Epon, and polymerized overnight at 60°C. One-micrometer sections were cut, stained with toluidine blue, and examined by light microscopy. Representative areas were chosen for electron microscopic study, and the Epon blocks were trimmed accordingly. Thin sections were cut with an LKB 8801 ultramicrotome and diamond knife, stained with lead citrate, and examined in an FEI Morgagni transmission electron microscope.

Quantification of lymphoblast storage material

EM images were blindly acquired by an experienced EM technologist, who, to reduce the chance of bias, was instructed to take whole-cell images at ×1200 magnification of the first 20 to 30 cells encountered during imaging, in which the nucleus was bisected at the plane of section. Blinded quantification of lymphocyte storage material was then carried out. The total number of vacuoles per lymphocyte with NCL-like storage material (defined by the presence of multilamellar, fingerprint profile storage material or the granular osmiophilic deposit profile storage material) was determined. Simultaneously, regions of interest around each vacuole containing storage material were traced, and the summed area of storage material–containing vacuoles per lymphocyte was determined.

Quantification of cathepsin activity (fluorescent-based and cathepsin D activity assay)

Human-derived fibroblasts (HDFs) were passaged into 10- or 15-cm tissue culture–treated culture dishes, allowed to expand to confluency, and cultured in 10% fetal bovine serum (FBS)/Dulbecco's modified Eagle's medium (DMEM) for 1 month. For experiments, 0.25% trypsin-EDTA solution was used to dissociate cells, and the cells were plated in 100-μl aliquots to a density of 2000 cells per well in TPP 96-well tissue culture plates. After adhesion of cells for 24 hours, the medium was removed from wells, and a probe, BMV109, was added to each well (0.25 μM BMV109 in 100 μl of FBS/DMEM). The probe was incubated with cells for 2 hours, after which point the probe-containing medium was removed, and wells were washed with nonfluorescent DMEM three times. Cells were incubated with Hoechst stain (1.6 μM) in nonfluorescent DMEM. The plates were imaged at ×10 magnification on Cellomics ArrayScan, with an exposure of 1 s. Two channels were used for imaging: 386 nm for nuclear stain and 650 nm for BMV109. The signal was quantified after imaging with Cellomics software using Cell Health Profiling. Wells with no probe were used as blanks. For cathepsin D activity assays, a fluorometric cathepsin D assay kit was used (BioVision). Briefly, HDFs were lysed with CD lysis buffer, incubated on ice for 10 min, and clarified via centrifugation at 16,000*g* for 5 min, and total protein levels were normalized across samples. Lysates were added to the master assay mix, mixed, and incubated for 1 hour at 37°C. Fluorescence was read on a fluorescent plate reader (excitation, 328 nm; emission, 460 nm).

In vivo retinal imaging in mice

All animals were maintained in full-barrier facilities free of specific pathogens on a 12-hour light/dark cycle with food and water ad libitum. Experiments were conducted in compliance with the ARVO (Association for Research in Vision and Ophthalmology) Statement for the Use of Animals in Ophthalmic and Visual Research, and all protocols were approved by the Institutional Animal Care and Use Committee at the University of California, San Francisco (#AN087501-02A). *Grn* knockout mice were fully backcrossed into C57BL/6J, and WT mice of the same genetic background served as controls. Mice were anesthetized with a steady flow of 1.5 to 3% isofluorane, eyes were anesthetized with propacaine, dilated with 1% tropicamide and 2.5% phenylephrine, and corneas were kept moist with 2.5% methylcellulose. A contact lens was placed over the mouse eye to improve the optics of the system. Retinal images were taken with a modified confocal scanning laser ophthalmoscope/OCT device (Heidelberg Spectralis, Heidelberg Engineering). After assuring centered beam placement by infrared cSLO and 90° position of the retina to the beam in the vertical and horizontal planes by OCT, autofluorescent retinal images were then taken at 457-nm excitation and 500-nm long-pass filter detection using TruTrack eye-tracking software, averaging at least 80 frames for each image, followed by OCT volume scans (100 automatic real-time, high resolution) through selected areas of interest.

Retinal lipofuscin quantification in mice

Eyes were enucleated and fixed in 4% paraformaldehyde overnight. Retinas were dissected out and mounted between slides and coverslips in a whole-mount configuration. Five separate fields of view, equally spaced around the perimeter of the retina, were imaged in each retina, located about 500 μm from the peripheral edge of the retina. Full-thickness confocal images were obtained at 2-μm step sizes using a Nikon Spinning Disk confocal microscope in the green fluorescent protein channel to image autofluorescent lipofuscin deposits. Individual lipofuscin deposits were marked with the cell counter feature by a blinded technician,

and the total number of lipofuscin deposits per z-stack was quantified. The average number of lipofuscin deposits per z-stack across all five fields of view was determined for each mouse.

Human retinal imaging

After pupillary dilation with 1% tropicamide ophthalmic solutions (Akorn), study participants underwent retinal autofluorescence imaging with a cSLO and OCT (Heidelberg Spectralis). cSLO imaging was performed using the standard autofluorescence settings of the device using TruTrack eye-tracking software, averaging at least 80 frames for each image. Trained technologists who were blinded to the mutation status acquired the images using standardized illumination and gain settings. Image quality was assessed by a blinded neuro-ophthalmologist, and only eyes with in-focus retinal images of sufficient quality to assess for the presence or absence of lipofuscin were analyzed further. Blinded quantification of retinal lipofuscin was performed jointly by a neuro-ophthalmologist (A.J.G.) and behavioral neurologist (M.E.W.). For each eye, the number of individual lipofuscin deposits was counted, and regions of interest were drawn around each lipofuscin deposit. The total number of lipofuscin deposits and the summed area of lipofuscin deposits were then calculated for each eye.

Quantification of lipofuscin in postmortem human cortical tissue

Formalin-fixed, paraffin-embedded, deidentified postmortem human frontal cortex and cervical spinal cord from heterozygous *GRN* mutation carriers, AD subjects, and age-similar and sex-similar control subjects without a clinical or pathological diagnosis of neurodegenerative disease were obtained from the University of British Columbia, the UCSF Neurodegenerative Disease Brain Bank, and Northwestern University. The work was deemed not human-subjects research per UCSF Committee on Human Research guidelines. 7.5-μm-thick sections were cut, dewaxed, and counterstained with DAPI (4′,6-diamidino-2-phenylindole). Autofluorescence imaging of lipofuscin and imaging of Sudan black–stained sections was performed by a blinded technician using a 20× objective and Cy5 filter set and bright field. Six to 30 nonoverlapping fields of view of superficial cortex were imaged, and regions of interest were drawn around lipofuscin deposits via an automated algorithm (Volocity software). The total area of cortex occupied by lipofuscin deposits was then calculated for each field of view. For EM analysis of storage material from postmortem human cortex, formalin-fixed cortex was post-fixed in EM fixative and processed for EM analysis, as above. Quantification of the percentage of neurons with lysosomal storage deposits and number of lysosomal storage deposits per cell was performed blindly.

Statistics

We used unpaired two-tailed *t* tests for normally distributed data and Mann-Whitney *U* tests for nonparametric data in experiments in which two comparison groups were involved. In experiments in which more than two comparison groups were involved, we used an ANOVA test with post hoc testing. A mixed-effects multivariable linear regression analysis, when used, accounted for intramouse and intraindividual variability. Statistical testing was performed using Stata 12.0 and Prism 6.

SUPPLEMENTARY MATERIALS

www.sciencetranslationalmedicine.org/cgi/content/full/9/385/eaah5642/DC1

Fig. S1. Increased lipofuscin in retinas from aged $Grn^{-/-}$ but not $Grn^{+/-}$ mice.

Fig. S2. Increased subunit C deposition in retinas of $Grn^{-/-}$ mice.

Fig. S3. Progranulin-deficient microglia accumulate NCL-like lysosomal storage material.

Fig. S4. EM analysis of postmortem spinal cord from control subjects and heterozygous *GRN* mutation carriers.

Fig. S5. Increased NCL-like storage material in lymphoblasts from heterozygous *GRN* mutation carriers versus sibling controls.

Fig. S6. Reduced cysteine cathepsin protease activity and cathepsin D activity in HDFs from heterozygous *GRN* mutation carriers versus sibling controls.

Table S1. Patient characteristics and quantification of human retinal autofluorescence imaging.

Table S2. Patient characteristics and quantification of human OCT macular cross-sectional scans.

Table S3. Data values for small sample sizes.

REFERENCES AND NOTES

1. E. D. Roberson, Frontotemporal dementia. *Curr. Neurol. Neurosci. Rep.* **6**, 481–489 (2006).
2. M. Baker, I. R. Mackenzie, S. M. Pickering-Brown, J. Gass, R. Rademakers, C. Lindholm, J. Snowden, J. Adamson, A. D. Sadovnick, S. Rollinson, A. Cannon, E. Dwosh, D. Neary, S. Melquist, A. Richardson, D. Dickson, Z. Berger, J. Eriksen, T. Robinson, C. Zehr, C. A. Dickey, R. Crook, E. Mcgowan, D. Mann, B. Boeve, H. Feldman, M. Hutton, Mutations in progranulin cause tau-negative frontotemporal dementia linked to chromosome 17. *Nature* **442**, 916–919 (2006).
3. J. Xu, M. Xilouri, J. Bruban, J. Shioi, Z. Shao, I. Papazoglou, K. Vekrellis, N. K. Robakis, Extracellular progranulin protects cortical neurons from toxic insults by activating survival signaling. *Neurobiol. Aging* **32**, 2326.e5–2326.e16 (2011).
4. C. L. Ryan, D. C. Baranowski, B. P. Chitramuthu, S. Malik, Z. Li, M. Cao, S. Minotti, H. D. Durham, D. G. Kay, C. A. Shaw, H. P. J. Bennett, A. Bateman, Progranulin is expressed within motor neurons and promotes neuronal cell survival. *BMC Neurosci.* **10**, 130 (2009).
5. P. Van Damme, A. Van Hoecke, D. Lambrechts, P. Vanacker, E. Bogaert, J. Van Swieten, P. Carmeliet, L. Van Den Bosch, W. Robberecht, Progranulin functions as a neurotrophic factor to regulate neurite outgrowth and enhance neuronal survival. *J. Cell Biol.* **181**, 37–41 (2008).
6. J. Gass, W. C. Lee, C. Cook, N. Finch, C. Stetler, K. Jansen-West, J. Lewis, C. D. Link, R. Rademakers, A. Nykjaer, L. Petrucelli, Progranulin regulates neuronal outgrowth independent of Sortilin. *Mol. Neurodegener.* **7**, 33 (2012).
7. Z. Ahmed, H. Sheng, Y.-F. Xu, W.-L. Lin, A. E. Innes, J. Gass, X. Yu, H. Hou, S. Chiba, K. Yamanouchi, M. Leissring, L. Petrucelli, M. Nishihara, M. L. Hutton, E. Mcgowan, D. W. Dickson, J. Lewis, Accelerated lipofuscinosis and ubiquitination in granulin knockout mice suggest a role for progranulin in successful aging. *Am. J. Pathol.* **177**, 311–324 (2010).
8. L. H. Martens, J. Zhang, S. J. Barmada, P. Zhou, S. Kamiya, B. Sun, S.-W. Min, L. Gan, S. Finkbeiner, E. J. Huang, R. V. Farese Jr., Progranulin deficiency promotes neuroinflammation and neuron loss following toxin-induced injury. *J. Clin. Invest.* **122**, 3955–3959 (2012).
9. A. S. Laird, A. Van Hoecke, L. De Muynck, M. Timmers, L. Van Den Bosch, P. Van Damme, W. Robberecht, Progranulin is neurotrophic in vivo and protects against a mutant TDP-43 induced axonopathy. *PLOS ONE* **5**, e13368 (2010).
10. F. Yin, R. Banerjee, B. Thomas, P. Zhou, L. Qian, T. Jia, X. Ma, Y. Ma, C. Iadecola, M. F. Beal, C. Nathan, A. Ding, Exaggerated inflammation, impaired host defense, and neuropathology in progranulin-deficient mice. *J. Exp. Med.* **207**, 117–128 (2010).
11. B. Cenik, C. F. Sephton, B. Kutluk Cenik, J. Herz, G. Yu, Progranulin: A proteolytically processed protein at the crossroads of inflammation and neurodegeneration. *J. Biol. Chem.* **287**, 32298–32306 (2012).
12. M. E. Ward, B. L. Miller, Potential mechanisms of progranulin-deficient FTLD. *J. Mol. Neurosci.* **45**, 574–582 (2011).
13. M. E. Ward, A. Taubes, R. Chen, B. L. Miller, C. F. Sephton, J. M. Gelfand, S. Minami, J. Boscardin, L. H. Martens, W. W. Seeley, G. Yu, J. Herz, A. J. Filiano, A. E. Arrant, E. D. Roberson, T. W. Kraft, R. V. Farese, A. Green, L. Gan, Early retinal neurodegeneration and impaired Ran-mediated nuclear import of TDP-43 in progranulin-deficient FTLD. *J. Exp. Med.* **211**, 1937–1945 (2014).
14. B. P. Hafler, Z. A. Klein, Z. Jimmy Zhou, S. M. Strittmatter, Progressive retinal degeneration and accumulation of autofluorescent lipopigments in Progranulin deficient mice. *Brain Res.* **1588**, 168–174 (2014).
15. A. J. Filiano, L. H. Martens, A. H. Young, B. A. Warmus, P. Zhou, G. Diaz-Ramirez, J. Jiao, Z. Zhang, E. J. Huang, F.-B. Gao, R. V. Farese, E. D. Roberson, Dissociation of frontotemporal dementia–related deficits and neuroinflammation in progranulin haploinsufficient mice. *J. Neurosci.* **33**, 5352–5361 (2013).
16. T. Petkau, S. Neal, A. Milnerwood, A. Mew, Synaptic dysfunction in progranulin-deficient mice. *Neurobiol. Dis.* **72**, 711–722 (2011).
17. K. R. Smith, J. Damiano, S. Franceschetti, S. Carpenter, L. Canafoglia, M. Morbin, G. Rossi, D. Pareyson, S. E. Mole, J. F. Staropoli, K. B. Sims, J. Lewis, W.-L. Lin, D. W. Dickson,

H.-H. Dahl, M. Bahlo, S. F. Berkovic, Strikingly different clinicopathological phenotypes determined by progranulin-mutation dosage. *Am. J. Hum. Genet.* **90**, 1102–1107 (2012).
18. L. Canafoglia, M. Morbin, V. Scaioli, D. Pareyson, L. D'Incerti, V. Fugnanesi, F. Tagliavini, S. F. Berkovic, S. Franceschetti, Recurrent generalized seizures, visual loss, and palinopsia as phenotypic features of neuronal ceroid lipofuscinosis due to progranulin gene mutation. *Epilepsia* **55**, e56–e59 (2014).
19. M. R. Almeida, M. C. Macário, L. Ramos, I. Baldeiras, M. H. Ribeiro, I. Santana, Portuguese family with the co-occurrence of frontotemporal lobar degeneration and neuronal ceroid lipofuscinosis phenotypes due to progranulin gene mutation. *Neurobiol. Aging* **41**, 200.e1–200.e5 (2016).
20. A. Jalanko, T. Braulke, Neuronal ceroid lipofuscinoses. *Biochim. Biophys. Acta* **1793**, 697–709 (2009).
21. G. W. Anderson, H. H. Goebel, A. Simonati, Human pathology in NCL. *Biochim. Biophys. Acta* **1832**, 1807–1826 (2013).
22. F. Yin, M. Dumont, R. Banerjee, Y. Ma, H. Li, M. T. Lin, M. F. Beal, C. Nathan, B. Thomas, A. Ding, Behavioral deficits and progressive neuropathology in progranulin-deficient mice: A mouse model of frontotemporal dementia. *FASEB J.* **24**, 4639–4647 (2010).
23. H. Lui, J. Zhang, S. R. Makinson, M. K. Cahill, K. W. Kelley, H.-Y. Huang, Y. Shang, M. C. Oldham, L. H. Martens, F. Gao, G. Coppola, S. A. Sloan, C. L. Hsieh, C. C. Kim, E. H. Bigio, S. Weintraub, M.-M. Mesulam, R. Rademakers, I. R. Mackenzie, W. W. Seeley, A. Karydas, B. L. Miller, B. Borroni, R. Ghidoni, R. V. Farese Jr., J. T. Paz, Ben A Barres, E. J. Huang, Progranulin deficiency promotes circuit-specific synaptic pruning by microglia via complement activation. *Cell* **165**, 921–935 (2016).
24. M. Verdoes, K. Oresic Bender, E. Segal, W. A. van der Linden, S. Syed, N. P. Withana, L. E. Sanman, M. Bogyo, Improved quenched fluorescent probe for imaging of cysteine cathepsin activity. *J. Am. Chem. Soc.* **135**, 14726–14730 (2013).
25. K. A. Vossel, A. J. Beagle, G. D. Rabinovici, H. Shu, S. E. Lee, G. Naasan, M. Hegde, S. B. Cornes, M. L. Henry, A. B. Nelson, W. W. Seeley, M. D. Geschwind, M. L. Gorno-Tempini, T. Shih, H. E. Kirsch, P. A. Garcia, B. L. Miller, L. Mucke, Seizures and epileptiform activity in the early stages of Alzheimer disease. *JAMA Neurol.* **70**, 1158–1166 (2013).
26. F. Hu, T. Padukkavidana, C. B. Vægter, O. A. Brady, Y. Zheng, I. R. Mackenzie, H. H. Feldman, A. Nykjaer, S. M. Strittmatter, Sortilin-mediated endocytosis determines levels of the frontotemporal dementia protein, progranulin. *Neuron* **68**, 654–667 (2010).
27. C. Cruchaga, C. Graff, H.-H. Chiang, J. Wang, A. L. Hinrichs, N. Spiegel, S. Bertelsen, K. Mayo, J. B. Norton, J. C. Morris, A. Goate, Association of TMEM106B gene polymorphism with age at onset in granulin mutation carriers and plasma granulin protein levels. *Arch. Neurol.* **68**, 581–586 (2011).
28. A. M. Nicholson, N. A. Finch, A. Wojtas, M. C. Baker, R. B. Perkerson III, M. Castanedes-Casey, L. Rousseau, L. Benussi, G. Binetti, R. Ghidoni, G.-Y. R. Hsiung, I. R. Mackenzie, E. Finger, B. F. Boeve, N. Ertekin-Taner, N. R. Graff-Radford, D. W. Dickson, R. Rademakers, TMEM106B p.T185S regulates TMEM106B protein levels: Implications for frontotemporal dementia. *J. Neurochem.* **126**, 781–791 (2013).
29. B. M. Schwenk, C. M. Lang, S. Hogl, S. Tahirovic, D. Orozco, K. Rentzsch, S. F. Lichtenthaler, C. C. Hoogenraad, A. Capell, C. Haass, D. Edbauer, The FTLD risk factor TMEM106B and MAP6 control dendritic trafficking of lysosomes. *EMBO J.* **33**, 450–467 (2013).

Acknowledgments: We thank J. Herz, L. Mitic, and R. Pearlman for their helpful feedback and A. Karydas for assistance in genetic testing of study participants and for help in obtaining lymphoblastoid cell lines. We thank the Program in Membrane Biology Microscopy Core at Massachusetts General Hospital and A. Simas for technical assistance in some of the lymphoblastoid EM studies. S. Arnow assisted in human retinal imaging. **Funding:** This study was funded by NIH (K08EY023610), Bluefield Foundation, American Brain Foundation (to M.E.W.); That Man May See (AW141505 and AW121324), Research to Prevent Blindness (Core), and National Eye Institute (PAR 13-269) (to A.J.G.); NIH (R01AG036884 and R01AG051390) and Consortium for Frontotemporal Dementia Research (to L.G.); NIH grant R01 NS098516, VA Merit Awards I01 RX002133 and I01 BX001108, and Consortium for Frontotemporal Dementia Research (to E.J.H.); NIH: National Institute of Neurological Disorders and Stroke (R01NS073813) (to S.L.C.); Alzheimer's Disease Center P30 A.13854 (to E.B. and M.-M.M.) and P30 AG13854 (to M.-M.M.); Philippe Foundation (to H.B.); National Multiple Sclerosis Society (FG 20102-A-1) (to A.C.-H.); and Consortium for Frontotemporal Dementia Research and NIH grants AG023501 and AG19724 (to W.W.S.). **Author contributions:** Experimental design: M.E.W., R.C., M.T., J.M.G., S.L.C., L.G., and A.J.G. Collection of data: M.E.W., R.C., H.-Y.H., C.L., A.T., C.C., S.L., H.B., S.S.M., P.A., A.C.-H., M.V.A., and J.F.S. Data analysis and interpretation: M.E.W., R.C., H.-Y.H., C.C., S.L., M.T., A.T., H.B., M.R., J.M.G., A.C.-H., M.V.A., W.W.S., B.L.M., J.F.S., E.J.H., L.G., and A.J.G. Subject recruitment: R.C., A.T., and W.W.S. Provision of reagents: W.W.S., I.R.M., J.F.S., E.B., M.-M.M., M.S.B., S.L.C., and E.J.H. Writing of the manuscript: M.E.W., L.G., and A.J.G. **Competing interests:** L.G. has received honoraria from Sanford Burnham Prebys Medical Discovery Institute. W.W.S. has received consulting fees from Merck Inc. J.M.G. has received consulting fees from Genentech and MedImmune, medical legal consulting, and research support from Genentech, Quest Diagnostics, and MedDay. P.A. has received speaker honoraria, consultation fees, or travel support from Allergan, Biogen, Eisai, GlaxoSmithKline, Ipsen, Merz, Novartis, and Teva and research grants from Biogen, Ipsen, Merz, Novartis, and Roche. B.L.M. serves as the medical director for the John Douglas French Alzheimer's Foundation; the scientific director for the Tau Consortium; the director/medical advisory board member of the Larry L. Hillblom Foundation; a scientific advisory board member for the National Institute for Health Research Cambridge Biomedical Research Centre and its subunit, the Biomedical Research Unit in Dementia (U.K.); and a board member for the American Brain Foundation. A.J.G. is a founder of Inception 5 Biosciences and is on the scientific advisory board of Bionure. All other authors declare that they have no competing interests.

Submitted 8 October 2014
Resubmitted 14 July 2016
Accepted 21 November 2016
Published 12 April 2017
10.1126/scitranslmed.aah5642

Citation: M. E. Ward, R. Chen, H.-Y. Huang, C. Ludwig, M. Telpoukhovskaia, A. Taubes, H. Boudin, S. S. Minami, M. Reichert, P. Albrecht, J. M. Gelfand, A. Cruz-Herranz, C. Cordano, M. V. Alavi, S. Leslie, W. W. Seeley, B. L. Miller, E. Bigio, M.-M. Mesulam, M. S. Bogyo, I. R. Mackenzie, J. F. Staropoli, S. L. Cotman, E. J. Huang, L. Gan, A. J. Green, Individuals with progranulin haploinsufficiency exhibit features of neuronal ceroid lipofuscinosis. *Sci. Transl. Med.* **9**, eaah5642 (2017).

Individuals with progranulin haploinsufficiency exhibit features of neuronal ceroid lipofuscinosis

Michael E. Ward, Robert Chen, Hsin-Yi Huang, Connor Ludwig, Maria Telpoukhovskaia, Ali Taubes, Helene Boudin, Sakura S. Minami, Meredith Reichert, Philipp Albrecht, Jeffrey M. Gelfand, Andres Cruz-Herranz, Christian Cordano, Marcel V. Alavi, Shannon Leslie, William W. Seeley, Bruce L. Miller, Eileen Bigio, Marek-Marsel Mesulam, Matthew S. Bogyo, Ian R. Mackenzie, John F. Staropoli, Susan L. Cotman, Eric J. Huang, Li Gan and Ari J. Green (April 12, 2017)

Science Translational Medicine **9** (385), . [doi: 10.1126/scitranslmed.aah5642]

Editor's Summary

Connecting the dots in neurodegenerative disease

Heterozygous *GRN* mutations lead to progranulin haploinsufficiency and cause frontotemporal dementia (FTD) in the elderly population, whereas homozygous *GRN* mutations cause neuronal ceroid lipofuscinosis (NCL), a lysosomal storage disease that mainly affects children. The underlying relationship between progranulin-deficient FTD and NCL remains unexplored. Now, Ward *et al*. show that patients with heterozygous *GRN* mutations exhibit clinical and pathological features that are strikingly similar to NCL. Like NCL patients, individuals with heterozygous *GRN* mutations accumulate storage material throughout the central nervous system, and their cells exhibit signs of lysosomal dysfunction. These findings implicate lysosomal dysfunction as a central mechanism in both *GRN*-associated FTD and NCL.

Science Translational Medicine (print ISSN 1946-6234; online ISSN 1946-6242) is published weekly, except the last week in December, by the American Association for the Advancement of Science, 1200 New York Avenue, NW, Washington, DC 20005.